Nano Research 2014, 7(1): 110–118
DOI 10.1007/s12274-013-0378-7
Research Article

ISSN 1998-0124
CN 11-5974/O4

Enhanced electrochemical performance in lithium ion batteries of a hollow spherical lithium-rich cathode material synthesized by a molten salt method

Xin He, Jun Wang, Richard Kloepsch, Steffen Krueger, Haiping Jia, Haidong Liu, Britta Vortmann, and Jie Li (✉)

MEET Battery Research Center / Institute of Physical Chemistry, University of Muenster, Corrensstrasse 46, D-48149 Muenster, Germany

Received: 28 August 2013
Revised: 14 October 2013
Accepted: 15 October 2013

KEYWORDS

Li-rich cathode,
nano hollow sphere,
molten salt synthesis,
electrochemical performance,
lithium ion batteries

ABSTRACT

A high voltage layered $Li_{1.2}Ni_{0.16}Co_{0.08}Mn_{0.56}O_2$ cathode material with a hollow spherical structure has been synthesized by molten-salt method in a NaCl flux. Characterization by X-ray diffraction and scanning electron microscopy confirmed its structure and proved that the as-prepared powder is constituted of small, homogenously sized hollow spheres (1–1.5 μm). The material exhibited enhanced rate capability and high first cycle efficiency due to the good dispersion of secondary particles. Galvanostatic cycling at different temperatures (20, 40, and 60 ˚C) and a current rate of 2 C (500 mA·g^{-1}) showed no significant capacity fade.

1 Introduction

As mobile storage of electric energy plays an increasingly important role in today's life, lithium-ion batteries (LIBs) have attracted a great deal of worldwide interests due to their high energy and power densities, safety and long applicable cycle life [1]. These advanced chemical power sources supply consumer electronic devices, portable power tools [2, 3], as well as large-scale applications such as electric vehicles (EVs), hybrid electric vehicles (HEVs) and stationary storage stations [4]. The cathode materials utilized in lithium-ion batteries greatly determine the energy storage capability. Therefore, considerable efforts have been devoted to the development of low-cost and high-energy cathode materials. Up to now, $LiCoO_2$ has mainly been used in the 3C market (computers, communication and consumer electronics), whereas layered $LiMO_2$ (M = Ni, Co, Mn, etc.), spinel $LiMn_2O_4$ and olivine $LiFePO_4$

Address correspondence to jie.li@uni-muenster.de

have been successfully commercialized in applications in EVs and HEVs [5, 6]. However, insufficient energy densities, as the result of low cathode capacities, limit the performance of today's LIBs, which are unable to fully satisfy the growing demand. In order to meet future requirements, many research activities now focus on high-capacity layered Li-rich oxide cathode materials, which can be written either as a solid solution $Li[Li_{x/3}Ni_{\alpha(1-x)}Co_{\beta(1-x)}Mn_{2x/3+\gamma(1-x)}]O_2$ or a nano-composite material $xLi_2MnO_3{\cdot}(1-x)LiMO_2$ (M = Ni, Co, Mn), known as Li-rich nickel cobalt manganese oxide (NCM). This kind of cathode material can deliver a discharge capacity f over 250 $mAh{\cdot}g^{-1}$ in the voltage range of 2.0–4.8 V at 0.1 C [7–12].

Although layered Li-rich cathodes may provide remarkably high specific capacities, their practical application is still limited due to major unsolved issues, such as (i) oxygen release during initial charge and hence serious safety problems, (ii) phase transformation from layered to spinel-layered intergrowth structure can result in continuous decay of the discharge plateau during long-term cycling, and (iii) Ni dissolution accompanied by increase in oxidation states of the remaining transition metals, at surface regions of Li-rich NCM particles [13–17].

To circumvent these obstacles, various strategies have been developed, especially regarding the materials synthesis. A feasible strategy is to retain the particle size within the nanometer scale [18], since smaller particles provide shorter diffusion pathways for ions as well as faster electron transport [19, 20].

In addition to this, a well-defined morphology, composition and interior micro-/nanostructures may also improve the electrochemical performance of cathode materials [21]. Nanostructured hollow spheres constitute one of the most promising particle morphologies, as they provide (i) enhanced specific capacities, which originate from extra active sites for the storage of Li^+ within the hollow cavities, (ii) an improved rate capability, which results from the large surface area of the nanoparticles [22, 23], (iii) an enhanced structural stability due to the void space within each sphere, which can buffer the local volume changes upon charge/discharge [24]. For instance, the syntheses of $LiNi_{0.5}Mn_{1.5}O_4$ [25] and $0.3Li_2MnO_3{\cdot}0.7LiNi_{0.5}Mn_{0.5}O_2$ [23] with spherical morphologies have been reported, and have proved that a hollow-structured material can provide enhanced electrochemical performance, especially in terms of their remarkable high rate capability. However, the "hollow-sphere" materials published to date are often strongly agglomerated and the electrochemical performance of the material is thereby limited.

In order to control the structural homogeneity and afford a narrow secondary particle size distribution during the synthesis [26], the molten-salt method is introduced in this work [27]. NaCl melts below 800 °C and provides a liquid reaction environment (flux). As a result, the required annealing temperature is reduced and the resulting particles are better dispersed compared to those obtained by a solid-state reaction. Meanwhile, during the reaction, one of the precursors is insoluble in the molten-salt medium, while the remaining ions can dissolve. Therefore, the morphology of the insoluble precursor can be preserved.

In this paper, a facile sacrificial-template approach to synthesize hollow-spherical structured $Li_{1.2}Ni_{0.16}Co_{0.08}Mn_{0.56}O_2$ at high temperature within a molten salt is reported. The structure, morphology and electrochemical performance of the synthesized material are extensively investigated. The electrodes prepared from these microspheres exhibit high capacity, excellent cycle stability, superior rate capability and high 1st cycle coulombic efficiency at both 20 °C and elevated temperatures of 40 °C and 60 °C.

2 Experimental

2.1 Material synthesis

$MnCO_3$ microspheres were prepared via a precipitation method as a template precursor. $MnSO_4$ solution (0.0285 mol/L), prepared in a water/ethanol (9:1 by volume) solvent mixture, was first precipitated by a NH_4HCO_3 solution (0.0285 mol/L) under continuous stirring at room temperature for 1 h. The as-obtained white $MnCO_3$ microspheres were thoroughly washed and dried in a vacuum oven at 80 °C overnight. The $MnCO_3$ microspheres were then calcined at 400 °C for 5 h in air at a heating rate of 1 $°C{\cdot}min^{-1}$ to prepare the corresponding MnO_2 microspheres [23].

$Li_{1.2}Ni_{0.16}Co_{0.08}Mn_{0.56}O_2$ hollow microspheres (LNCM synthesized with NaCl: From this point onward abbreviated as MS-LNCM) were synthesized by a molten-salt method. In this method, NaCl has been chosen as the molten-salt flux. Stoichiometric amounts of $Ni(NO_3)_2{\cdot}6H_2O$, $Co(NO_3)_2{\cdot}6H_2O$, as-prepared MnO_2 microspheres, and 2 mol% excess of $LiOH{\cdot}H_2O$ were mixed with NaCl in a weight ratio of 1:3 and then dispersed in acetone. After that, the acetone was slowly evaporated at 50 ℃ with stirring and the mixture was calcined at 800 ℃ for 15 h in air. After cooling to room temperature, the powder was first washed with deionized water and then dried at 100 ℃ overnight to remove residual water. For comparison, $Li_{1.2}Ni_{0.16}Co_{0.08}Mn_{0.56}O_2$ was also synthesized by the same procedure without the addition of molten salt (LNCM without NaCl: NMS-LNCM).

2.2 Morphology and structural characterization

The crystal structure of the powders was characterized by X-ray diffraction (XRD) in a 2θ-range of 10°–90° with a step size of 0.01°/step, which was performed on a Bruker D8 Advance diffractometer (Germany) using Cu K_α radiation. The lattice parameters were determined by Rietveld refinement using the Maud 2.0 software package [28]. Particle morphology was evaluated using field-emission scanning electron microscopy (FE-SEM, Zeiss Auriga). A focused-ion beam (FIB-SEM) study was carried out to investigate the interior of the obtained spheres. Elemental mapping was carried out by energy dispersive X-ray analysis (EDX; Oxford Instruments). The Li:Ni:Co:Mn-ratio as well as the Na content of the materials were also analyzed by inductively-coupled plasma optical-emission spectrometry (ICP–OES). The specific surface area was determined by the Brunauer–Emmett–Teller (BET) method by physisorption of nitrogen (Micromeritics ASAP 2020).

2.3 Electrochemical investigation

Electrodes were prepared by casting a slurry with the composition of 80 wt.% $Li_{1.2}Ni_{0.16}Co_{0.08}Mn_{0.56}O_2$ active material, 10 wt.% Super C65 (Timcal) carbon black and 10 wt.% polyvinylidene difluoride (PVDF) (KynarFlex®761A), onto an aluminum foil. The slurry was prepared by magnetic stirring for 12 h in order to preserve the integrity of the hollow spheres. The active material mass loading was about 2.5 mg/cm^2. The electrodes were assembled into CR2032-type coin cells with lithium metal as counter electrode and 1 M $LiPF_6$ in 1:1 ethylene carbonate:dimethyl carbonate (EC:DMC; wt./wt.) as electrolyte.

Galvanostatic cycling was carried out on MACCOR series 4000 battery testers in the voltage range 2.0–4.8 V at different current rates (1 C = 250 mA·g^{-1}). The elevated temperature performance was evaluated by cycling the cells at three different temperatures of 20, 40, and 60 °C.

3 Results and discussion

Scheme 1 illustrates the synthesis procedure of the hollow MS-LNCM microspheres. The porous MnO_2 microspheres were obtained through thermal decomposition treatment of $MnCO_3$ at 400 ℃ for 5 h according to [23]

$$2MnCO_3 + O_2 \longrightarrow 2MnO_2 + 2CO_2$$

Upon mixing, Li^+, Ni^{2+}, Co^{2+} migrate into or surround the resulting porous MnO_2. When the annealing temperature reaches 800 ℃, NaCl melts and serves as a molten-salt flux during the sintering process. After drying, decomposition and lithiation through an *in situ* sacrificial-template route, LNCM microspheres were obtained. The reactions can described as below

$$LiOH{\cdot}H_2O \longrightarrow LiOH + H_2O$$

$$4MnO_2 \longrightarrow 2Mn_2O_3 + O_2$$

$$2Ni(NO_3)_2{\cdot}6H_2O \longrightarrow 2NiO + 4NO_2 + 12H_2O + O_2$$

$$2Co(NO_3)_2{\cdot}6H_2O \longrightarrow 2CoO + 4NO_2 + 12H_2O + O_2$$

$$30LiOH + 7Mn_2O_3 + 4NiO + 2CoO + 4O_2 \longrightarrow 25Li_{1.2}Ni_{0.16}Co_{0.08}Mn_{0.56}O_2 + 15H_2O$$

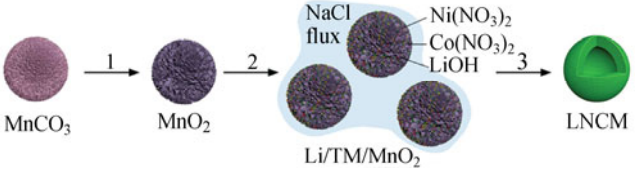

Figure 1 Schematic route for the synthesis of $Li_{1.2}Ni_{0.16}Co_{0.08}Mn_{0.56}O_2$ hollow microspheres.

Since MnO_2 is insoluble in molten NaCl, good contact exists between the porous MnO_2 template spheres and the Li/Ni/Co-salts. Therefore, crystal growth and particle morphology of MS-LNCM material are controlled.

The XRD patterns and the Rietveld refinement results of the MS-LNCM and NMS-LNCM are shown in Fig. 2. Low reliability factors R_p (< 5%) demonstrate satisfactory refinements. Sharp XRD reflections indicate the high sample crystallinity. The peaks of both samples can be indexed on the basis of a hexagonal α-$NaFeO_2$ structure (space group: $R\bar{3}m$, No. 166) [29], except for a few broad peaks between 20° and 25°. These broad diffraction peaks are known to be caused by the $LiMn_6$ superlattice ordering within the transition metal slab of the monoclinic

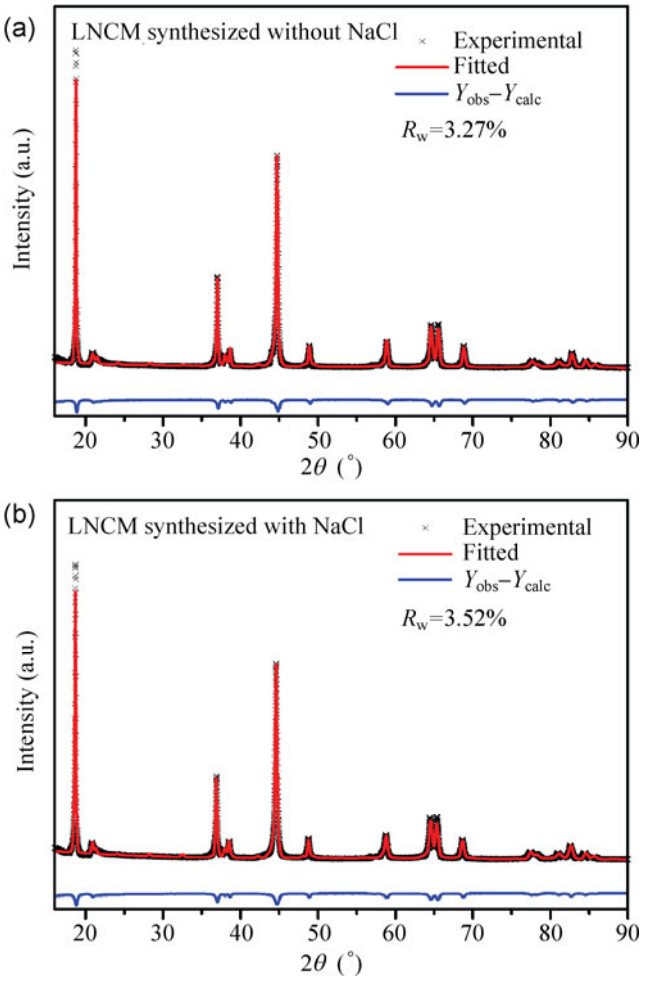

Figure 2 Observed, calculated and the difference XRD patterns of the $Li_{1.2}Ni_{0.16}Co_{0.08}Mn_{0.56}O_2$ samples synthesized (a) without and (b) with NaCl.

$Li[Li_{1/3}Mn_{2/3}]O_2$ entity (space group: C2/m, No. 12). Although the molten-salt method uses NaCl, calcination is carried out at lower temperatures and shorter times than conventional routes, and no impurity phases could be observed. The results of the compositional analysis shown in Table 1 prove that the experimental compositions of both samples are in good agreement with the target values, i.e. Li:Ni:Co:Mn = 1.20:0.16:0.08:0.56. Both samples contain traces of Na (~3.5 ppm), most likely originating from the starting agents. Thus, rinsing the sample with water is regarded as an efficient method to remove residual Na and to obtain pure LNCM microspheres.

Rietveld refinements were carried out to investigate the effect of using NaCl on the lattice parameters of synthesized materials. The software Maud 2.0 was used to perform the refinement based on two structural models ($R\bar{3}m$ and C2/m) and the results are listed in Table 1. The lattice parameters a, c and the resulting unit cell volume V of the MS-LNCM are slightly bigger than those of the NMS-LNCM, indicating that the material obtained from the molten-salt method facilitates intercalation and de-intercalation of lithium ions through a wider space of host structure. This may in turn result in enhanced electrochemical performance, especially regarding rate capability.

Particle morphologies of precursors and final product were investigated by SEM (Fig. 3). Figures 3(a) and 3(b) show the SEM images of $MnCO_3$ and MnO_2 precursors. Both samples have a spherical morphology with secondary particle size in the range of 1–1.5 μm. These microspherical particles are composed of primary nanoparticles with triangular shape. After high temperature annealing, the primary particle shape changes from triangular to round, while the spherical morphology of secondary particle was preserved (Fig. 3(c)). Similar to the precursors, the size of these spheres also range within 1–1.5 μm. That is to say, the synthesis approach and high temperature annealing do not alter the morphology of the secondary particle in both size and shape. According to the Kirkendall effect, during the sacrificial-template process, Mn, Ni, and Co atoms rapidly diffuse outward and the opposite O atoms slowly diffuse inward, which leads to the formation of the void within the LNCM microspheres [30]. Only

Table 1 The lattice parameters obtained from Rietveld refinement and ICP–OES analysis results of NMS-LNCM and MS-LNCM. The structural parameters are denoted according to the hexagonal R$\bar{3}$m phase.

Sample		MS-LNCM	NMS-LNCM
XRD refinement	*a* (nm)	0.2854(2)	0.2851(9)
	c (nm)	1.4216(3)	1.4202(9)
	R$\bar{3}$m:C2/m (Phase ratio %)	47:53	35:65
ICP–OES	Li:Ni:Co:Mn (molar ratio)	1.20:0.16:0.09:0.56	1.20:0.16:0.08:0.54
	Na content (ppm)	3.53	3.46

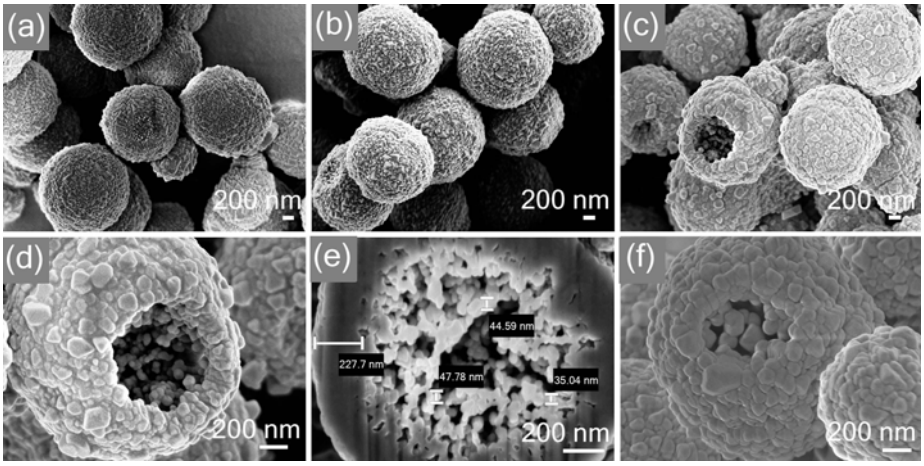

Figure 3 SEM images of (a) $MnCO_3$, (b) MnO_2, (c) and (d) MS-LNCM, (e) FIB-SEM image of MS-LNCM, and (f) SEM image of NMS-LNCM.

a few hollow particles could be directly identified by their self-formed surface hole (Fig. 3(d)). The internal cavity within the majority of microspheres is confirmed in Fig. 3(e), obtained by creating a particle cross section using combined focused-ion beam SEM, in which the particle split in half by the Ga ion beam is shown. Generally, the individual secondary particles of this material have a typical hollow structure with a rough surface. The walls of these hollow spheres have a thickness of approximately 220 nm, while the internal diameter is below 50 nm. The presence and homogenous distribution of Ni, Co, and Mn inside the hollow microspheres was identified by EDX chemical mapping of a halved sphere, as showed in Fig. 4. After high temperature treatment, the Ni and Co can readily migrate from the sphere surface to the inside structure, consistent with the XRD results, which once again confirms the purity of the synthesized material.

An interesting difference between the MS-LNCM and NMS-LNCM shows in the surface area analysis: MS-LNCM has a much higher surface area of 14.21 $m^2 \cdot g^{-1}$ than NMS-LNCM (1.19 $m^2 \cdot g^{-1}$). Such a high surface area will surely result in an enhanced electrochemical performance, especially the rate capability. In order to elucidate the cause of the large difference in surface area, low magnification SEM images of both materials are compared in Fig. 5. As can be seen, the hollow microspheres form in both synthesis approaches with very similar size. However, Fig. 5(a) shows that NMS-LNCM microspheres are strongly agglomerated, while the MS-LNCM microspheres are loosely distributed and much less agglomerated (Fig. 5(b)). The different degree of agglomeration therefore explains the large difference in BET surface areas. The larger specific surface area of the material MS-LNCM also facilitates electrolyte wetting of the resulting electrode. However, the high surface area may also result in low volumetric energy density. Thus, the tap densities of MS-LNCM and NMS-LNCM are worth measuring before practical application. In addition, the high magnification SEM

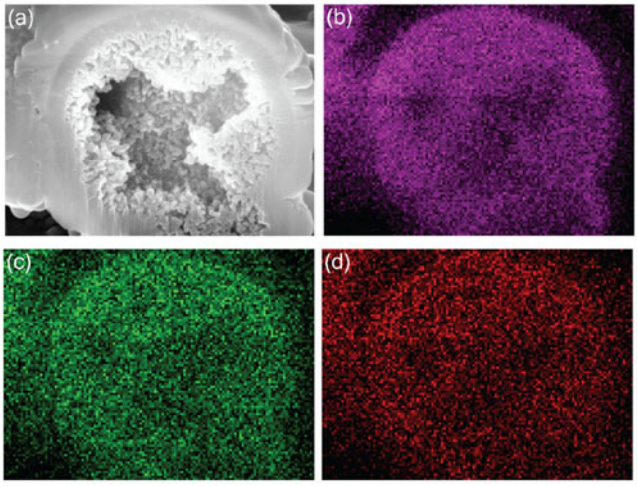

Figure 4 SEM/EDX electron image (a) and element mapping of Mn (b), Ni (c), Co (d) in a halved hollow spherical MS-LNCM particle.

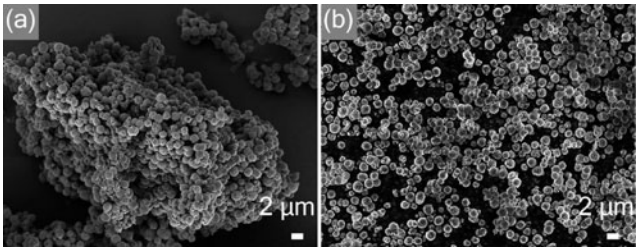

Figure 5 SEM images of (a) NMS-LNCM and (b) MS-LNCM in the low magnification.

image of NMS-LNCM, shown in Fig. 3(f), indicates that the hollow shell of this material is obviously thicker than that of MS-LNCM, and a larger number of separate primary particles are located inside the hollow spheres. This structure will surely lead to worse electrochemical performance, especially at high current rate.

In order to identify the influence of the different morphology on the electrochemical performance, the electrochemical properties of the two LNCM materials were initially investigated by rate tests carried out at 40 °C (Fig. 6). The cells were first charged and discharged between 2.0–4.8 V at current densities of 0.1, 0.2, 1, 2, 5, and 20 C, respectively with 3 cycles at each rate. MS-LNCM delivers discharge capacities of 296, 279, 244, 226, 199, and 144 mAh·g^{-1}, respectively, at 0.1, 0.2, 1, 2, 5, and 20 C. As can be seen in Fig. 6(a), these capacities are obviously higher than for NMS-LNCM. The performance difference becomes more apparent with increasing current densities. For example, at 0.1 C the discharge capacity of NMS-LNCM lies still well above 250 mAh·g^{-1}, which is more than 80% of the capacity delivered by MS-LNCM. However, this capacity dramatically decreases to 44 mAh·g^{-1} at 20 C, which is less than 30% than for NMS-LNCM. For a convenient comparison of the obtained capacities a histogram of the capacity ratio at each current rate is shown in Fig. 5(b). The data points are labeled according to the ratio of the 2nd cycle discharge capacity between MS-LNCM and NMS-LNCM. In other words, MS-LNCM displays a good electrochemical performance in both specific capacity and rate capability. After the rate test, the cells were further cycled at 0.1 C for 3 cycles and 2 C for 40 cycles. As can be seen, when the charge and discharge rate change back to 0.1 C after 18 cycles, the reversible discharge capacity delivered by the MS-LNCM returned to 284 mAh·g^{-1}, which is similar to the initial cycle. It provides a reversible capacity as high as 230 mAh·g^{-1} without obvious capacity fade within 40 cycles at 2 C, which again demonstrates the good rate capability and stable cycling performance of this material. The physical properties of the LNCM materials synthesized by the two methods indicate that the larger lattice parameters, the better dispersion of the secondary particles, and the improved electrochemical performance of MS-LNCM can be attributed to the higher BET surface area of the LNCM material.

The temperature-dependence of the electrochemical performance at 20 and 60 °C of MS-LNCM was also tested under the same procedure as Fig. 6 and the results are plotted together with the one at 40 °C in Fig. 7. It is known that a higher operating temperature leads to higher specific capacities for Li-rich cathode materials, regardless of the current density applied. All three cells exhibit good cycling retention and stable cycling performance after the rate test, although the two cells tested at elevated temperature (40 and 60 °C) showed slight fading due to electrolyte decomposition [31]. At ambient temperature, where electrolyte decomposition is less likely to occur, no fading could be observed in within test cycles. Nevertheless, high reversible capacities of 180, 230, and 250 mAh·g^{-1} at 20, 40, and 60 °C at 2 C could be obtained. To the best of our knowledge, such high capacities with good retention at this current rate

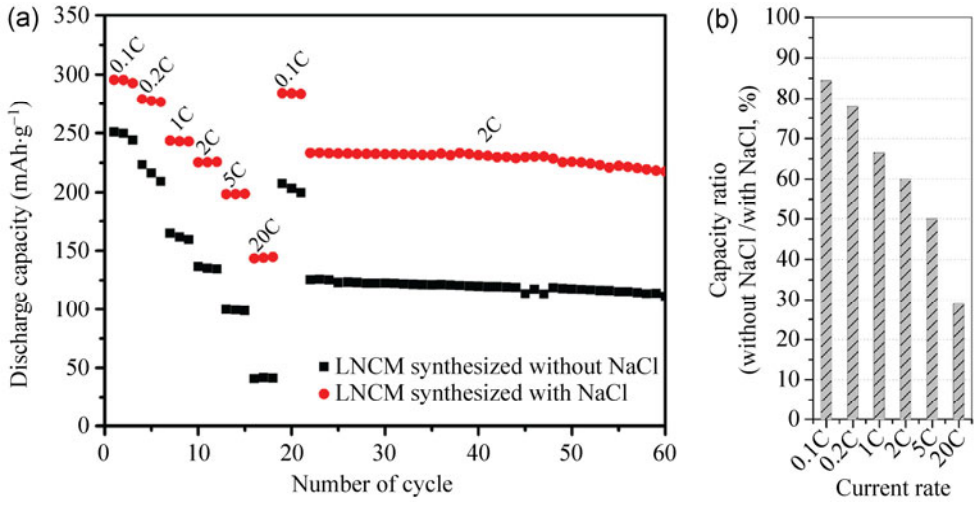

Figure 6 (a) Comparison of rate capability of the $Li_{1.2}Ni_{0.16}Co_{0.08}Mn_{0.56}O_2$ electrodes synthesized with and without NaCl cycled at 40 °C. (b) The ratio between the discharge capacities of electrode composed of MS-LNCM and NMS-LNCM materials at different current densities.

have not been reported so far, especially at elevated temperature. Once again, the well-dispersed, hollow-spherical LNCM cathode material presented in this work displays very good electrochemical performance regarding specific capacity, rate capability and cycling stability, independent of the chosen operating temperature (20, 40, or 60 ℃).

Last of all, it is worth commenting on the difference of first cycle coulombic efficiency between NMS-LNCM and MS-LNCM. For this reason, the first cycle charge/discharge voltage profiles and the corresponding $dQ \cdot dV^{-1}$-plots of both cells cycled at 0.1C and 40 ℃ are compared in Figs. 8(a) and 8(b), respectively. It can be seen that the MS-LNCM has a much higher 1st cycle coulombic efficiency of 92% than the one NMS-LNCM (80%). In practical applications, this will be a very promising property in terms of cathode/anode electrode balancing. Fig. 8(a) shows that both profiles exhibit two plateaus during the first charge, due to the existence of two different processes which arise from lithium de-insertion from the $R\bar{3}m$ and C2/m phase region [32], respectively. Compared to NMS-LNCM, the voltage profile of MS-LNCM shows an obviously longer first slope and shorter second plateau. The sloping lower voltage region (< 4.4 V) corresponds to the reversible extraction of Li^+ ions from $R\bar{3}m$ region with the concomitant oxidation of Ni^{2+} to Ni^{4+} and Co^{3+} to Co^{4+}, which corresponds to the oxidation peak at approximately 4.0 V in the $dQ \cdot dV^{-1}$-plot. The long voltage plateau (~4.5 V) is widely accepted to be attributed to an irreversible loss of oxygen from the manganese-rich C2/m region and the transformation into a MnO_2-like phase. According to the phase ratio determined by Rietveld refinement shown in Table 1, the material prepared by the molten-salt route contains a higher amount of $R\bar{3}m$ phase (47%) than the one without molten salt (35%), even though ICP–OES analysis had indicated an identical elemental composition. This finding agrees well with the progression of the charge voltage profiles (Fig. 8(a)), in which MS-LNCM

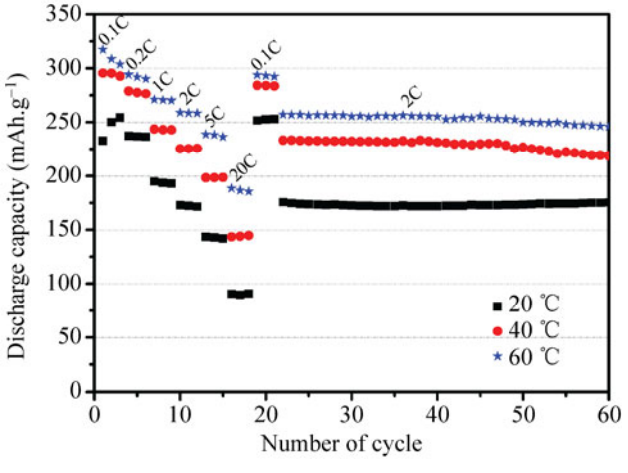

Figure 7 temperature-dependent rate capabilities of the $Li_{1.2}Ni_{0.16}Co_{0.08}Mn_{0.56}O_2$ electrodes obtained by the NaCl-assisted synthesis method cycled at 20, 40, and 60 °C.

shows a higher capacity in the lower voltage region (< 4.4 V). Since the Li-rich materials do not clearly show distinct redox features in the voltage profiles after initial charge, a $dQ \cdot dV^{-1}$ plot is used to visualize the different processes and is plotted in Fig. 8(b). The peak between 3.5–4.5 V can be assigned to the redox activity of Ni/Co. It shows a similar trend to that of the charging process, i.e. the peak maximum of MS-LNCM is slightly higher than for NMS-LNCM. However, the second peak at 3.3 V, which originates from lithiation of the newly formed MnO_2 phase shows the opposite behavior. The peak maximum of MS-LNCM is significantly higher than for NMS-LNCM, even although the amount of MnO_2 present should be much less-based on the phenomenon of the 1st charging process. In other words, the relative amount of electrochemically active MnO_2 is higher in MS-LNCM. This may be due to the good dispersion of secondary particles within the material synthesized with the assistance of the molten salt and it is worthy of further investigation.

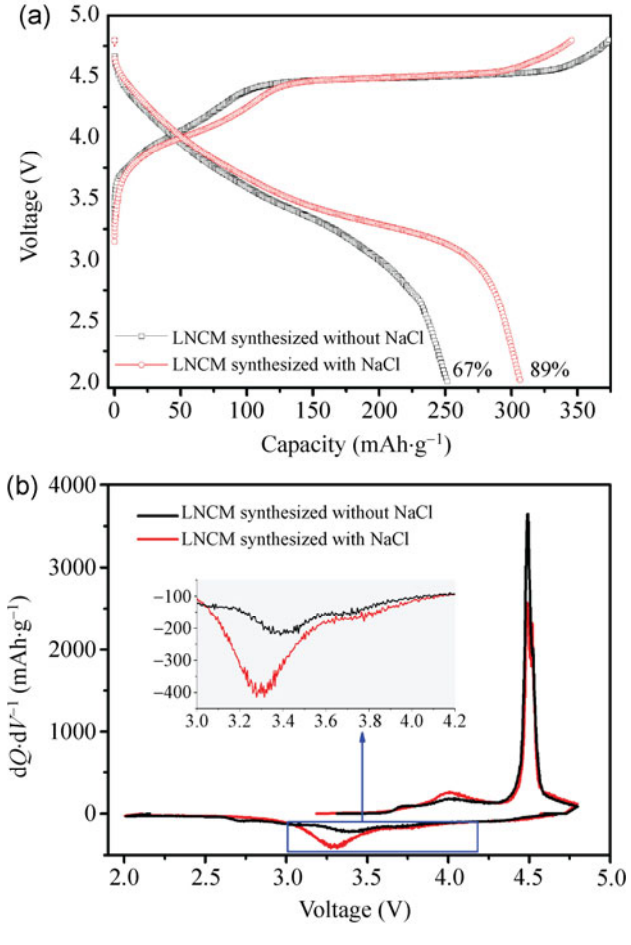

Figure 8 Comparison of the 1st cycle charge/discharge voltage profiles (a) and the corresponding $dQ \cdot dV^{-1}$ plot (b) of LNCM synthesized with and without NaCl. Both cells were tested between 2.0–4.8 V at 0.1 C.

4 Conclusions

Well-crystallized $Li_{1.2}Ni_{0.16}Co_{0.08}Mn_{0.56}O_2$ hollow micro spheres have been successfully synthesized by a molten-salt method. SEM and surface area analysis prove that the $Li_{1.2}Ni_{0.16}Co_{0.08}Mn_{0.56}O_2$ microspheres preserve their hollow spherical morphology in the NaCl-assisted synthesis and display a larger specific surface area than the material synthesized without molten salt. The resulting material provides extra active sites for Li^+ storage and much better secondary particle dispersion. This results in very promising electrochemical properties, such as a high specific capacity, good rate capability, stable cycling behavior and a high 1st cycle coulombic efficiency.

Acknowledgements

The authors kindly acknowledge the financial support of the Federal Ministry of Education and Research (BMBF), the Federal Ministry of Economic and Technology (BMWi) and the Federal Ministry for the Environment, Nature Conservation and Nuclear Safety (BMU) of Germany within the project KaLiPat.

References

[1] Tarascon, J. M.; Armand, M. Issues and challenges facing rechargeable lithium batteries. *Nature* **2001**, *414*, 359–367.

[2] Besenhard, J. O.; Winter, M. Insertion reactions in advanced electrochemical energy storage. *Pure Appl. Chem.* **1998**, *70*, 603–608.

[3] Winter, M.; Besenhard, J. O. Wiederaufladbare batterien. *Chem. Unserer Zeit* **1999**, *33*, 252–266.

[4] Wagner, R.; Preschitschek, N.; Passerini, S.; Leker, J.; Winter, M. Current research trends and prospects among the various materials and designs used in lithium-based batteries. *J. Appl. Electrochem.* **2013**, *43*, 481–496.

[5] Ohzuku, T.; Brodd, R. J. An overview of positive-electrode materials for advanced lithium-ion batteries. *J. Power Sources* **2007**, *174*, 449–456.

[6] Chen, Z. H.; Dahn, J. R. Reducing carbon in $LiFePO_4$/C

composite electrodes to maximize specific energy, volumetric energy, and tap density. *J. Electrochem. Soc.* **2002**, *149*, A1184–A1189.

[7] Lu, Z. H.; MacNeil, D. D.; Dahn, J. R. Layered cathode materials $Li[Ni_xLi_{(1/3-2x/3)}Mn_{(2/3-x/3)}]O_2$ for lithium-ion batteries. *Electrochem. Solid-State Lett.* **2001**, *4*, A191–A194.

[8] Shin, S. S.; Sun, Y. K.; Amine, K. Synthesis and electrochemical properties of $Li[Li_{(1-2x)/3}Ni_xMn_{(2-x)/3}]O_2$ as cathode materials for lithium secondary batteries. *J. Power Sources* **2002**, *112*, 634–638.

[9] Johnson, C. S.; Kim, J. S.; Lefief, C.; Li, N.; Vaughey, J. T.; Thackeray, M. M. The significance of the Li_2MnO_3 component in "composite" $xLi_2MnO_3\cdot(1-x)LiMn_{0.5}Ni_{0.5}O_2$ electrodes. *Electrochem. Comm.* **2004**, *6*, 1085–1091.

[10] Wu, Y.; Manthiram, A. High capacity, surface-modified layered $Li[Li_{(1-x)/3}Mn_{(2-x)/3}Ni_{x/3}Co_{x/3}]O_2$ cathodes with low irreversible capacity loss. *Electrochem. Solid-State Lett.* **2006**, *9*, A221–A224.

[11] Zheng, J. M.; Zhang, Z. R.; Wu, X. B.; Dong, Z. X.; Zhu, Z.; Yang, Y. The effects of AlF_3 coating on the performance of $Li[Li_{0.2}Mn_{0.54}Ni_{0.13}Co_{0.13}]O_2$ positive electrode material for lithium-ion battery. *J. Electrochem. Soc.* **2008**, *155*, A775–A782.

[12] Wang, J.; He, X.; Paillard, E.; Liu, H. D.; Passerini, S.; Winter, M.; Li, J. Improved rate capability of layered Li-rich cathode for lithium ion battery by electrochemical treatment. *ECS Electrochem. Lett.* **2013**, *2*, A78–A80.

[13] Kumai, K.; Miyashiro, H.; Kobayashi, Y.; Takei, K.; Ishikawa, R. Gas generation mechanism due to electrolyte decomposition in commercial lithium-ion cell. *J. Power Sources* **1999**, *81–82*, 715–719.

[14] Kong, W. H.; Li, H.; Huang, X. J.; Chen, L. Q. Gas evolution behaviors for several cathode materials in lithium-ion batteries. *J. Power Sources* **2005**, *142*, 285–291.

[15] Holzapfel, M.; Würsig, A.; Scheifele, W.; Vetter, J.; Novák, P. Oxygen, hydrogen, ethylene and CO_2 development in lithium-ion batteries. *J. Power Sources* **2007**, *174*, 1156–1160.

[16] Kang, S. H.; Thackeray, M. M. Enhancing the rate capability of high capacity $xLi_2MnO_3\cdot(1-x)LiMO_2$ (M = Mn, Ni, Co) electrodes by Li–Ni–PO_4 treatment. *Electrochem. Comm.* **2009**, *11*, 748–751.

[17] Song, B. H.; Liu, Z. W.; Lai, M. O.; Lu, L. Structural evolution and the capacity fade mechanism upon long-term cycling in Li-rich cathode material. *Phys. Chem. Chem. Phys.* **2012**, *14*, 12875–12883.

[18] Wei, G. Z.; Lu, X.; Ke, F. S.; Huang, L.; Li, J. T.; Wang, Z. X.; Zhou, Z. Y.; Sun, S. G. Crystal habit-tuned nanoplate material of $Li[Li_{1/3-2x/3}Ni_xMn_{2/3-x/3}]O_2$ for high-rate performance lithium-ion batteries. *Adv. Mater.* **2010**, *22*, 4364–4367.

[19] Shaju, K. M.; Bruce, P. G. A stoichiometric nano-$LiMn_2O_4$ spinel electrode exhibiting high power and stable cycling. *Chem. Mater.* **2008**, *20*, 5557–5562.

[20] Guo, Y. G.; Hu, J. S.; Wan, L. J. Nanostructured materials for electrochemical energy conversion and storage devices. *Adv. Mater.* **2008**, *20*, 2878–2887.

[21] Zhou, L.; Zhao, D. Y.; Lou, X. W. Double-shelled $CoMn_2O_4$ hollow microcubes as high-capacity anodes for lithium-ion batteries. *Adv. Mater.* **2012**, *24*, 745–748.

[22] Ding, S. J.; Chen, J. S.; Wang, Z. Y.; Cheah, Y. L.; Madhavi, S.; Hu, X.; Lou, X. W. TiO_2 hollow spheres with large amount of exposed (001) facets for fast reversible lithium storage. *J. Mater. Chem.* **2011**, *21*, 1677–1680.

[23] Jiang, Y.; Yang, Z.; Luo, W.; Hu, X.; Huang, Y. Hollow $0.3Li_2MnO_3\cdot0.7LiNi_{0.5}Mn_{0.5}O_2$ microspheres as a high-performance cathode material for lithium-ion batteries. *Phys. Chem. Chem. Phys.* **2013**, *15*, 2954–2960.

[24] Qiao, Y.; Li, S. R.; Yu, Y.; Chen, C. H. Synthesis and electrochemical properties of high performance yolk-structured $LiMn_2O_4$ microspheres for lithium ion batteries. *J. Mater. Chem. A* **2013**, *1*, 860–867.

[25] Zhou, L.; Zhao, D. Y.; Lou, X. W. $LiNi_{0.5}Mn_{1.5}O_4$ hollow structures as high-performance cathodes for lithium-ion batteries. *Angew. Chem. Int. Ed.* **2012**, *51*, 239–241.

[26] Bareño, J.; Lei, C. H.; Wen, J. G.; Kang, S. H.; Petrov, I.; Abraham, D. P. Local structure of layered oxide electrode materials for lithium-ion batteries. *Adv. Mater.* **2010**, *22*, 1122–1127.

[27] Liu, J. L.; Chen, L.; Hou, M. Y.; Wang, F.; Che, R. C.; Xia, Y. Y. General synthesis of $xLi_2MnO_3\cdot(1-x)LiMn_{1/3}Ni_{1/3}Co_{1/3}O_2$ nanomaterials by a molten-salt method: Towards a high capacity and high power cathode for rechargeable lithium batteries. *J. Mater. Chem.* **2012**, *22*, 25380–25387.

[28] Lutterotti, L.; Matthies, S.; Chateigner, D.; Ferrari, S.; Ricote. J. Rietveld texture and stress analysis of thin films by X-ray diffraction. *Mater. Sci. Forum* **2002**, *408–412*, 1603–1608.

[29] Li, J.; Klöpsch, R.; Stan, M. C.; Nowak, S.; Kunze, M.; Winter, M.; Passerini, S. Synthesis and electrochemical performance of the high voltage cathode material $Li[Li_{0.2}Mn_{0.56}Ni_{0.16}Co_{0.08}]O_2$ with improved rate capability. *J. Power Sources* **2011**, *196*, 4821–4825.

[30] Zhang, X. Y.; Jiang, W. J.; Mauger, A.; Qilu, R.; Gendron, F.; Julien, C. M. Minimization of the cation mixing in $Li_{1+x}(NMC)_{1-x}O_2$ as cathode material. *J. Power Sources* **2010**, *195*, 1292–1301.

[31] Kawamura, T.; Okada, S.; Yamaki, J. I. Decomposition reaction of $LiPF_6$-based electrolytes for lithium ion cells. *J. Power Sources* **2006**, *156*, 547–554.

[32] Li, J.; Klöpsch, R.; Nowak, S.; Kunze, M.; Winter, M.; Passerini, S. Investigations on cellulose-based high voltage composite cathodes for lithium ion batteries. *J. Power Sources* **2011**, *196*, 7687–7691.